Nanoscale

ROYAL SOCIETY OF CHEMISTRY

PAPER

Published on 05 May 2025
Licence and permissions

Cite this: *Nanoscale*, 2025, **17**, 13298

Enhanced solar harvesting efficiency in nanostructured MXene monolayers based on scandium and yttrium†

Bill D. Aparicio-Huacarpuma, [a,b] Marcelo L. Pereira, Jr, [*c,d] Mauricio J. Piotrowski, [e] Celso R. C. Rêgo, [f] Diego Guedes-Sobrinho, [g] Luiz A. Ribeiro, Jr [a,b] and Alexandre C. Dias [h]

MXenes have garnered significant attention in nanoelectronics due to their tunable electronic properties. Such tunability makes them potential candidates for high-efficiency solar energy applications. Here, we investigate the structural, electronic, optical, and excitonic properties of 2D M_2CT_2 (M = Y, Sc; T = O, F, S, Cl, Se, Br, Te, I, H, OH) MXene monolayers using a computational protocol that combines first-principles and semi-empirical methods. By employing an automated workflow that integrates five distinct Workflow Active Nodes (WaNos) within the SimStack framework, we systematically assessed the structural stability and electronic properties of 22 candidate monolayers. This approach enhances computational efficiency and ensures reproducibility by adhering to FAIR and TRUE data principles. Phonon dispersion analysis revealed that ten systems are stable, five are metastable, and seven are unstable. Among the stable and metastable monolayers, we identified several semiconductors—Y_2CCl_2, Y_2CBr_2, Y_2CH_2, Y_2Cl_2, Sc_2CCl_2, Sc_2CBr_2, Sc_2CF_2, and Sc_2CH_2—with indirect Heyd–Scuseria–Ernzerhof (HSE06) band gaps ranging from 1.24–1.90 eV. Excitonic effects induced by quantum confinement contribute to exciton binding energies from 210–470 meV, consistent with typical 2D materials. Additionally, some monolayers demonstrate potential for solar harvesting applications, with predicted energy conversion efficiency approaching 30% under full photon absorption.

Received 31st December 2024,
Accepted 4th May 2025

DOI: 10.1039/d4nr05505e

rsc.li/nanoscale

1 Introduction

Since the experimental discovery of graphene in 2004,[1] 2D materials have gained considerable attention for their potential applications across several fields.[2] In the post-graphene era, other notable 2D materials, such as MXenes,[3] hexagonal boron nitride (h-BN),[4] black phosphorus (BP),[5] and transition metal dichalcogenides (TMDs),[6] have emerged. Among these, MXenes, discovered by Yury Gogotsi and collaborators in 2011,[3,7,8] are layered 2D transition metal carbides or nitrides, typically represented by the formula $M_{n+1}X_nT_x$, where M is a transition metal, X is carbon or nitrogen (with n = 1, 2, 3, or 4), and T_x represents surface terminations such as O, F, S, Cl, Se, Br, Te, I, H, or OH.[9–11] These materials have been applied in various domains, including supercapacitors,[12] environmental treatment,[13] catalysis and gas sensing,[14–17] energy storage,[18,19] ion batteries,[20] photovoltaic cells,[21,22] transparent flexible conductors,[23] and biomedical applications.[24]

The electronic properties of M_2C (M = Hf, Nb, Sc, Ta, Ti, V, Zr) MXenes were investigated demonstrating their metallic behavior, which holds promise for electronic devices.[25] Similarly, oxygen-functionalized MXenes were explored by highlighting their potential for energy and electronics applications.[26] Among the numerous MXene combinations, semiconductors such as Ti_2CO_2, Zr_2CO_2, Hf_2CO_2, and Sc_2CO_2 have shown promise for solar energy harvesting.[27] Machine learning

[a]*Institute of Physics, University of Brasília, 70910-900 Brasília, DF, Brazil*
[b]*Computational Materials Laboratory, LCCMat, Institute of Physics, University of Brasília, 70910-900 Brasília, DF, Brazil*
[c]*University of Brasília, College of Technology, Department of Electrical Engineering, University of Brasília, 70919-970 Brasília, DF, Brazil. E-mail: marcelo.lopes@unb.br*
[d]*Department of Materials Science and NanoEngineering, Rice University, 77005 Houston, TX, USA*
[e]*Department of Physics, Federal University of Pelotas, 96010-900 Pelotas, RS, Brazil*
[f]*Karlsruhe Institute of Technology (KIT), Institute of Nanotechnology, Hermann-von-Helmholtz-Platz, 76344 Eggenstein–Leopoldshafen, BW, Germany*
[g]*Chemistry Department, Federal University of Paraná, 81531-980 Curitiba, PR, Brazil*
[h]*Institute of Physics and International Center of Physics, University of Brasília, 70910-900 Brasília, DF, Brazil*

† Electronic supplementary information (ESI) available: We provide the PAW projectors with computational technical details, POSCARs of the crystal structures, phonon dispersion and thermodynamic potentials, electronic band structure, excitonic and optical properties, and detailed data on the solar harvesting efficiency of these monolayers. See DOI: https://doi.org/10.1039/d4nr05505e

models have also predicted semiconducting MXenes, providing a fast approach for identifying MXenes tailored for specific applications.[28] Despite these advances, the excitonic properties of MXenes remain relatively unexplored.

It was shown that quasi-particle (excitonic) effects play a crucial role in determining the solar energy harvesting efficiency of MXenes.[29] Recent studies have underscored the importance of excitonic properties in Hf-based MXenes.[30] Also, the relevance of electron–hole coupling in Sc- and Hf-based MXene semiconductors for tunable optoelectronic devices was demonstrated.[31] Nevertheless, studies on the solar energy harvesting efficiency of MXenes, mostly in Sc- and Y-based MXene semiconductors, are lacking in the literature, and the present work aims to fill this gap.

In this study, we present a theoretical investigation of the 2D M_2CT_2 (M = Y, Sc; T = O, F, S, Cl, Se, Br, Te, I, H, OH) MXene monolayers combining density functional theory (DFT) and a semi-empirical approach based on maximally localized Wannier function tight-binding (MLWF-TB) model.[32,33] We first use DFT to evaluate the ground state's thermodynamic stability and electronic properties, determining electronic band gaps. Several semiconducting materials with band gaps ranging from 1.25 eV to 1.90 eV were identified. The linear optical response allows us to analyze the impact of quasi-particle effects on absorption spectra. These results are further used to estimate the solar harvesting efficiency of the monolayers. We employed an automated workflow by integrating five distinct Workflow Active Nodes (WaNos) within the SimStack framework to systematize data acquisition and ensure the reproducibility of our findings.[34] This workflow allowed systematic assessment of the thermodynamic stability and electronic properties of 22 candidate monolayers, adhering to FAIR (Findable, Accessible, Interoperable, Reusable) and TRUE (Transparent, Reproducible, Usable by Others, Extensible)[34,35] data principles.

2 Methodology

All first-principles calculations were carried out within the framework of DFT,[36,37] using the Vienna *Ab initio* Simulation Package (VASP).[38] The Kohn–Sham (KS) equations were solved *via* the projector-augmented wave (PAW) method,[39] with the KS states expanded by using plane waves. The electronic and structural properties were described through the Perdew–Burke–Ernzerhof (PBE) exchange–correlation functional.[40] Given the known limitations of PBE in accurately describing electronic band gaps,[41,42] mainly due to self-interaction errors and poor treatment of weak interactions,[43] a more accurate description was obtained by employing the HSE06-screened Coulomb hybrid functional.[44]

For Brillouin zone (BZ) integration, a Γ-centered *k*-mesh of 12 × 12 × 1 was used for Y_2CT_2 and 14 × 14 × 1 for Sc_2CT_2 monolayers, and their non-functionalized counterparts, respectively, to compute structural and electronic properties. A vacuum layer of 24 Å to 32 Å was introduced in the non-periodic direction to eliminate interactions between periodic images, with thickness varying according to the MXene functionalization. Further details of the crystal structure setup and vacuum layer are provided in the ESI, section S2.† During structural optimization, the self-consistent cycle converged with a total energy criterion of 10^{-6} eV, and atomic forces were minimized to less than 0.01 eV $Å^{-1}$. A plane-wave energy cutoff of 800 eV was applied in all simulations.

Phonon dispersion calculations, utilizing density functional perturbation theory (DFPT),[45] were conducted to evaluate the thermodynamic stability of the MXene monolayers. These calculations were performed using the VASP + Phonopy package,[46] with a 2 × 2 × 1 supercell and a *k*-mesh consistent with those employed in the structural and electronic property computations. Visualization and structural analyses were carried out using VESTA software.[47]

The *ab initio* molecular dynamics simulations (AIMD) was made using FHI-aims code,[48,49] utilizing numerical atom-centered orbitals (NAOs) light first tier basis set. The AIMD simulations was made with PBE functional, with a 3 × 3 × 1 supercell with a 4 × 4 × 1 *k*-mesh. All simulations was done at NVT ensamble with Noosé–Hoover thermostat, at 300 K during 5 ps with a timestep of 1 fs.

The optical response, excitonic effects, and solar harvesting efficiency were investigated using the WanTiBEXOS code,[50] which solves the Bethe–Salpeter equation (BSE)[51] to account for excitonic quasi-particle effects. The MLWF-TB Hamiltonian, used to describe the single particle electron and hole states in WanTiBEXOS, was derived from HSE06 DFT calculations using Wannier90.[52] We included d orbital projections for Sc and Y; p projections for C, F, Cl, Br, and I; and s projections for H. The optical properties were computed using both the independent particle approximation (IPA, neglecting excitonic effects) and the BSE approaches, with a *k*-points density of 120 $Å^{-1}$ in the 2D plane. The lowest conduction band and three highest valence bands were considered, and smearing of 0.05 eV was applied in the dielectric function calculations at both IPA and BSE levels. The BSE calculations employed a 2D truncated Coulomb potential (V2DT)[53] to deal with the BSE electron–hole Coulomb potential.

The solar harvesting efficiency of the monolayers was estimated by computing the power conversion efficiency (PCE) based on the Shockley–Queisser limit,[54] which is a function of the band gap. Additionally, we employed the spectroscopy-limited maximum efficiency (SLME)[29] approach, accounting for the band gap's direct/indirect nature and the optical absorbance derived from the absorption coefficient. We used the AM1.5G solar spectrum model,[55] assuming an operating temperature of 300 K. The absorbance was derived from the total absorption coefficient, considering the dielectric function's diagonal components. The monolayer thickness was defined as the intrinsic material thickness plus the van der Waals (vdW) length (3.21 Å), following the procedure outlined in the ESI, Tables S5 and S6.† This method aligns with previous studies,[32,56–58] and was adopted based on the approach by Bernardi *et al.*,[59] where the vdW length was critical for accu-

rately estimating the absorbance of atomically thin materials such as graphene.

A schematic representation of the complete simulation protocol is shown in Fig. 1(a), where, in summary, all investigated MXenes were first structurally optimized using DFT with the PBE functional. The materials were then subjected to a stepwise and eliminative stability screening. Initially, phonon dispersion calculations were performed to identify and exclude dynamically unstable systems. The Born–Huang mechanical stability criterion was applied among the remaining candidates, discarding non-compliant structures. To verify their thermal stability, those that passed both filters were subsequently evaluated through AIMD. The systems deemed stable or metastable were then classified as metallic or semiconducting. Elect electronic and optical properties were calculated for the semiconducting ones, followed by their PCE estimation.

We generated our raw dataset integrating five distinct WaNos Workflow Active Nodes (WaNos) as shown in Fig. 2 within the SimStack framework.[34] This workflow began by constructing the initial M_2CT_2 (M = Y, Sc; T = O, F, S, Cl, Se, Br, Te, I, H, OH) MXene monolayer structures according to design principles. The configurations are available in our GitHub repository, where we also make available extra key data information to allow the reproducibility of our results in an automated data pipeline for processing and evaluation. A Colab notebook was employed to extract and share all post-processing data for structural and electronic properties, facilitating the assessment of structural stability, electronic band gaps, and excitonic features.

The Mult-It WaNo organizes and manages input data across the workflow, creating lists of floating-point numbers, integers, and filenames. This WaNo handles all POSCAR files from a given archive, and the UnpackMol WaNo processes all POSCAR files in the *Foreach* loop control. The UnpackMol WaNo decompresses and prepares configuration files, providing initial structures to the DFT-VASP WaNo, which carries out DFT calculations using the Vienna *Ab initio* Simulation Package (VASP).[38] This approach optimizes complex VASP calculations, allowing researchers to focus on the analysis of M_2CT_2 monolayers' structural and electronic stability. The DB-Generator WaNo creates comprehensive YAML files that

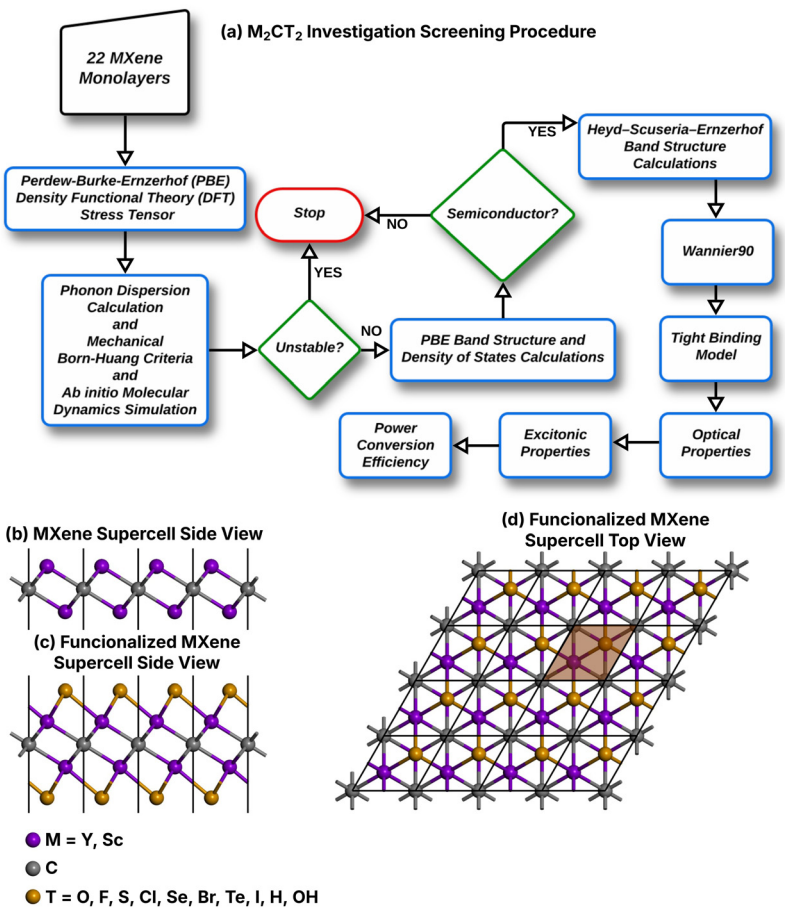

Fig. 1 (a) Screening procedure steps for the investigated M_2CT_2 MXene monolayers. (b) Side view of the supercell of MXene M_2C (M = Y or Sc) and (c) the MXene M_2CT_2 functionalized with T elements (T = O, F, S, Cl, Se, Br, Te, I, H, or OH), the vertical lines indicate the unit cell boundaries. (d) Top view of the functionalized 4 × 4 × 1 supercell of MXene M_2CT_2, with the unit cell of the nanomaterial highlighted in brown. The M, C, and T atoms are represented as purple, gray, and yellow spheres, respectively.

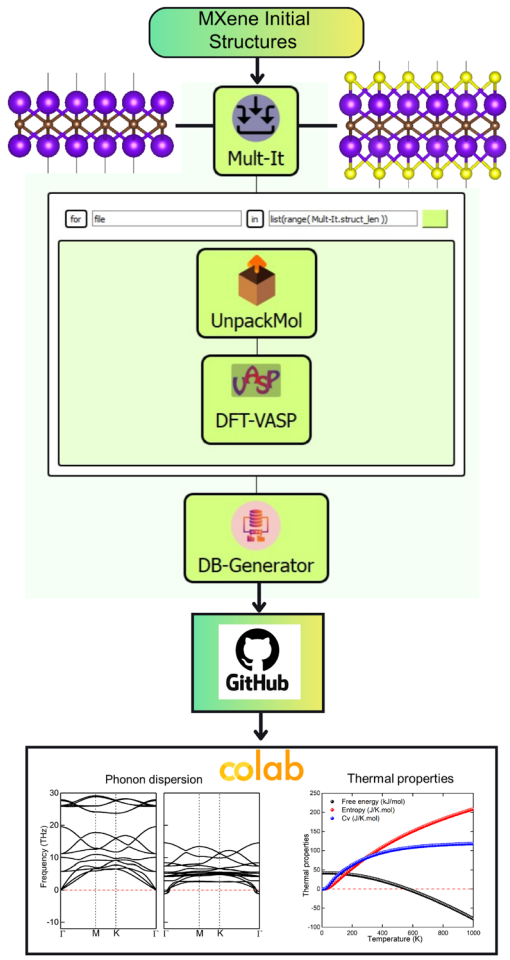

Fig. 2 Workflow employed for calculating the phonon dispersion and thermal properties of MXene monolayers. The workflow involves several components, each serving a specific function in the process: Mult-It: manages and organizes data lists; UnpackMol: prepares configuration files for DFT calculations; DFT-VASP: carries out Density Functional Theory calculations; DB-Generator: compiles the results into a *yml* file. Additionally, the workflow pushes the *yml* file to a GitHub repository to link the generated data with a Colab notebook, where the results of the simulations are visualized.

log total energies, key parameters from OUTCAR files, and detailed structural data for each MXene monolayer configuration. These files are essential in subsequent workflow stages, where data are automatically pushed to a GitHub repository and imported into a Colab notebook, forming a dataset for evaluating the thermal and optical properties of stable, metastable, and unstable configurations.

By adhering to FAIR (Findable, Accessible, Interoperable, Reusable) and TRUE (Transparent, Reproducible, Usable by Others, Extensible) data principles,[34,35] this workflow guarantees scalability, reproducibility, and flexibility. These principles enhance the reliability and accessibility of our findings, including excitonic binding energies and band gaps, which span 1.24 eV to 1.90 eV for several identified semiconductor compositions. All results presented below are based on raw data from our pipeline. Additional technical details on using our workflow and the Colab notebook are available in the same GitHub repository.

3 Results

This section presents the findings related to the MXenes investigated in this study. We begin by examining each system's stability. For (meta-)stable systems, we detail their electronic properties, categorizing them as metallic or semiconducting. In the case of semiconductors, we further explore their excitonic and optical characteristics, concluding with an analysis of their solar harvesting efficiency.

3.1 Structural stability

The crystal structures of M_2C and M_2CT_2 monolayers are schematically shown in Fig. 1(b)–(d). All MXene monolayers exhibit a trigonal crystal structure, with functionalization elements denoted by T. The lattice constants (a_0) and cohesive energies (E_{coh}) for these structures are listed in Table 1. The E_{coh} represents the energy (per atom) required to separate the constituent atoms into neutral, free atoms. Negative values of E_{coh} indicate a reduction in total energy upon crystal formation, suggesting the structure is energetically favorable. In contrast, positive values imply the crystal structure is not energetically favorable.

The cohesive energy is calculated using the following expression:[60–62]

$$E_{coh} = \frac{E_{tot}(M_2CT_2) - 2E(M) - E(C) - 2E(T)}{\text{number of atoms in the unit cell}}, \quad (1)$$

Table 1 Equilibrium lattice constant (a_0) and cohesive energy (E_{coh}) for the investigated MXene monolayers

System	E_{coh} [eV per atom]	a_0 [Å]
Y_2C	−5.55	3.12
Y_2CO_2	−6.31	3.22
Y_2CF_2	−6.10	3.57
Y_2CS_2	−5.23	3.84
Y_2CCl_2	−5.40	3.72
Y_2CBr_2	−5.13	3.77
Y_2CI_2	−4.77	3.87
Y_2CH_2	−4.57	3.59
$Y_2C(OH)_2$	−5.31	3.59
Y_2CSe_2	−4.96	3.77
Y_2CTe_2	−4.85	3.64
Sc_2C	−5.41	3.31
Sc_2CO_2	−6.23	3.22
Sc_2CF_2	−6.12	3.28
Sc_2CS_2	−5.19	3.52
Sc_2CCl_2	−5.37	3.44
Sc_2CBr_2	−5.07	3.52
Sc_2CI_2	−4.65	3.66
Sc_2CH_2	−4.63	3.29
$Sc_2C(OH)_2$	−5.34	3.30
Sc_2CSe_2	−5.04	3.32
Sc_2CTe_2	−4.90	3.42

where E_{tot} (M_2CT_2) represents the total energy of the MXene monolayer, and E(M), E(C), and E(T) are the total energies per atom for the metal (M = Y, Sc), carbon (C), and the functionalization element (T = O, F, S, Cl, Se, Br, Te, I, H, or OH), respectively. The unit cell of non-functionalized MXene monolayers contains three atoms, while functionalized monolayers typically contain five, except for OH-functionalized systems, which have seven atoms per unit cell.

For the Y-based systems, we found that only Y_2CO_2 (−6.10 eV per atom) and Y_2CF_2 (−6.10 eV per atom) exhibit lower E_{coh} values than Y_2C (−5.55 eV per atom), indicating higher energetic stability. In contrast, other functionalizations increase E_{coh}, up to the limit of −4.57 eV per atom for Y_2CH_2. A similar trend is observed in the Sc-based systems, with Sc_2C (−5.41 eV per atom) leading to E_{coh} higher only than T = O (−6.23 eV per atom) or F (−6.12 eV per atom), with the highest value obtained for T = H (−4.63 eV per atom). In all cases, Y-based systems have E_{coh} slightly higher than their Sc-based analogs.

Regarding the structural characteristics of the MXenes, as previously mentioned, all the systems reported here possess a trigonal crystal structure with lattice vectors of equal magnitude (in-plane) and angles of 90° and 120°. For the Y_2CT_2 systems, all ten functionalized MXenes have a larger a_0 than the non-functionalized Y_2C, where a_0 = 3.12 Å. In this case, the lattice constants range from 3.12 Å to 3.84 Å, following a clear trend where heavier functionalization elements correspond to larger lattice constants, increasing of up to 23% compared to the Y_2C system. However, this trend is not observed in the systems with M = Sc, where functionalizations such as T = O_2, F_2, H_2, or $(OH)_2$ result in smaller a_0 values than non-functionalized Sc_2C (a_0 = 3.31 Å). The lattice constants for the Sc-based systems range from 3.22 Å to 3.66 Å, showing variations from a 2.7% decrease to an 11% increase, indicating less variation than the Y-based systems.

The dynamic stability of the MXene monolayers was further investigated through the phonon dispersion profiles of each monolayer, allowing classification into stable, meta-stable, or unstable categories based on established criteria.[58,63] A system is considered stable if there are no imaginary frequencies in the phonon dispersion or if such frequencies are limited to the Γ point, with their magnitudes corresponding to less than 1% of the highest frequency for that monolayer. MXenes with imaginary frequencies with magnitudes less than or equal to 2 THz are classified as meta-stable. Monolayers that do not meet these criteria are classified as unstable. It is worth noting that the systems described here as (meta-)stable may have minor imaginary modes removed by applying slight strains to the monolayers.[64,65]

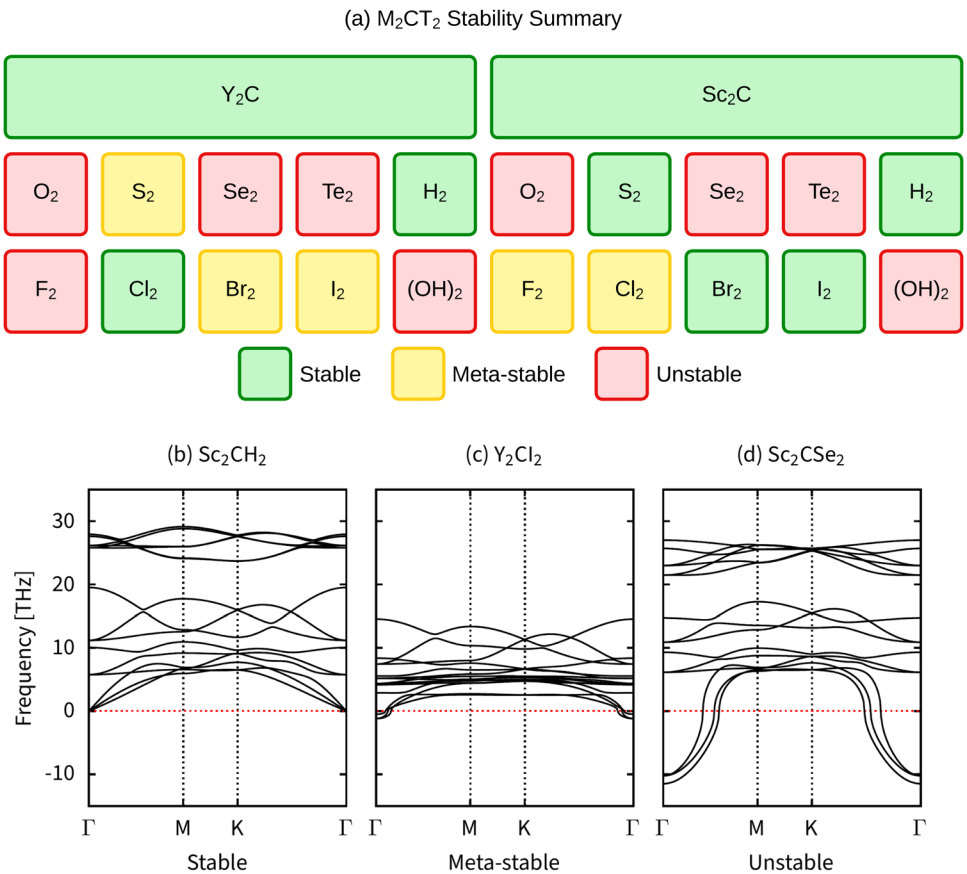

Fig. 3 (a) List of MXenes compositions, alongside representative phonon dispersion plots for (b) stable, (c) meta-stable, and (d) unstable systems: Sc_2CH_2, Y_2Cl_2, and Sc_2CSe_2, respectively.

Fig. 3(a) summarizes the stability classification of the MXene monolayers after applying all criteria considered in this study. Fig. 3(b–d) present representative phonon dispersion curves corresponding to stable, metastable, and unstable systems. Of the 22 MXene monolayers examined, ten were classified as stable, five as meta-stable, and seven as unstable. In the following sections, we will focus on the stable and meta-stable monolayers, omitting further discussion of the unstable systems. A complete set of phonon dispersion data for all 22 monolayers investigated here can be found in the ESI, section S3.†

For the stable and metastable monolayers we calculated their elastic constants, shown in Table 2, the entire group, except the monolayers with Te functionalization, satisfied the Born–Huang criterion: $C_{11}C_{22} - (C_{12})^2 > 0$ and $C_{66} > 0$, being considered mechanically stable. The angular dependent Young modulus and Poisson's ratio were provided in the ESI section S4.† Beyond the stability criteria, the elastic constants provide valuable insights into the mechanical behavior of the investigated systems, constituting an important complement to the physicochemical understanding of these materials and their potential technological applications. In addition to the fact that M_2CTe_2 systems are not mechanically stable, our results also indicate that, regardless of the surface functionalization, the TMD-based MXenes containing Y exhibit lower maximum Young's modulus (Y_{max}) compared to their Sc-based counterparts. Specifically, the pristine systems present Y_{max} values of approximately 80 N m^{-1} and 92 N m^{-1} for Y_2C and Sc_2C, respectively, in good agreement with the literature.[66]

Interestingly, surface functionalization can significantly modify Young's modulus, enhancing or reducing it. For the Y-based systems, Y_{max} ranges from approximately 27 N m^{-1} to 125 N m^{-1}, indicating a reduction of nearly 70% with *S* functionalization and an increase of almost 60% with H. For the Sc-based systems, the values range from 29 N m^{-1} to 161 N m^{-1}, with the lowest modulus also observed for *S* functionalization, while the highest enhancement is obtained with *F*. Regarding the maximum Poisson's ratio (ν_{max}), the values span from 0.16 to 0.48, encompassing both brittle and ductile mechanical responses. Due to the symmetry of the MXenes studied here, Young's modulus and Poisson's ratio exhibit relatively small variations from the reported maximum values.

In order to complement the stability analysis of these systems, we made AIMD simulations for the mechanically stable monolayers, as shown in Fig. 4. From these results, we observe that all systems has a total energy oscillation around an average value after the thermalization in the first picosecond, where the system was going from 0 K to 300 K, showing that all mechanically stable systems are thermodynamic stable at 300 K. The detailed results of AIMD showing the total energy variation and temperature variation, are shown in the ESI section S5.† After all calculations to identify the dynamical, mechanical, and thermodynamical stability of

Table 2 The elastic constants C_{ij} (N m^{-1}), maximun Young's modulus Y_{max}, and maximum Poisson's ratio ν_{max}. The Young's modulus is in units of N m^{-1}, while Poisson's ratio is dimensionless

System	C_{11} (N m^{-1})	C_{22} (N m^{-1})	C_{12} (N m^{-1})	C_{66} (N m^{-1})	Y_{max} (N m^{-1})	ν_{max}
Y_2C	82.82	82.82	15.32	33.13	79.99	0.19
Y_2CCl_2	122.95	122.95	33.88	44.62	113.75	0.28
Y_2CBr_2	110.97	110.97	28.34	41.13	103.73	0.26
Y_2CI_2	101.76	101.76	22.51	39.58	96.78	0.22
Y_2CH_2	129.49	129.49	26.05	52.25	125.01	0.20
Y_2CS_2	32.98	32.98	14.31	8.21	26.77	0.48
Y_2CTe_2	54.82	54.82	61.08	−3.71		
Sc_2C	94.50	94.50	15.41	39.80	92.33	0.16
Sc_2CF_2	168.77	168.77	36.20	66.39	161.16	0.21
Sc_2CCl_2	145.62	145.62	34.95	55.25	137.23	0.24
Sc_2CBr_2	141.8	141.8	36.66	52.53	132.32	0.26
Sc_2CI_2	123.28	123.28	31.73	47.48	117.77	0.26
Sc_2CH_2	156.68	156.68	32.54	61.27	149.92	0.21
Sc_2CS_2	29.57	29.57	3.42	11.79	29.17	0.17
Sc_2CTe_2	88.34	88.34	83.03	−1.20		

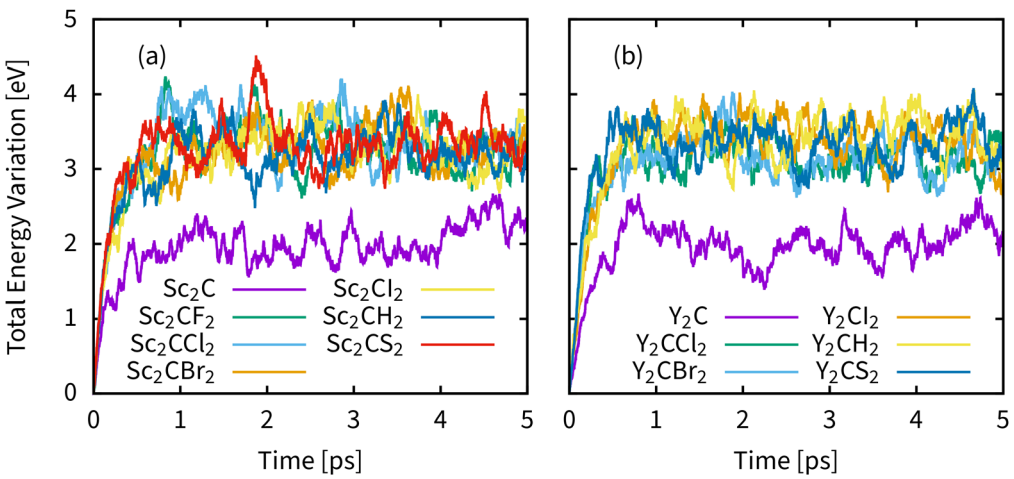

Fig. 4 Total Energy variation in AIMD simulations of (a) Sc_2C and (b) Y_2C and their respective functionalizations. All simulations were done at 300 K.

these monolayers, from the initial 22 monolayers, only 13 monolayers can be considered stable.

3.2 Electronic properties

By analyzing the electronic properties through the band structure and density of states (DoS), as shown in Fig. 5 and 6, we identified eight semiconductors and five metals among the 13 stable systems. These classifications are labeled in Fig. 5(c and f). Notably, the non-functionalized MXene monolayers (Y_2C and Sc_2C) display metallic behavior, indicating that functionalization is a mechanism for opening band gaps. The complete DoS and electronic band structure dataset is available in ESI, section S6.†

From the projected DoS, we observe that the primary contribution of Y and Sc atoms near the Fermi level comes from d-orbitals in both the valence and conduction bands, along with additional p-orbital contributions in the valence states.

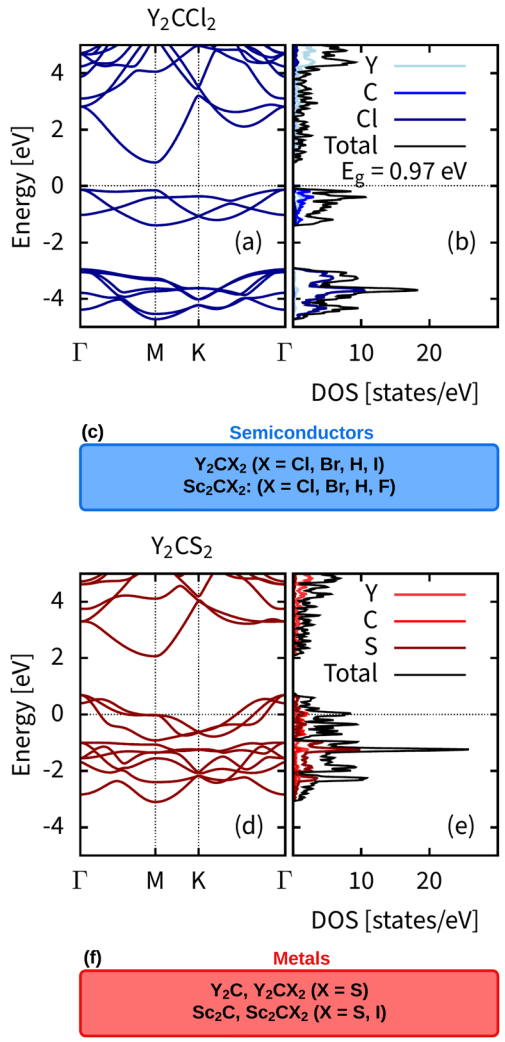

Fig. 5 (a) PBE band structure and (b) total density of states for the semiconducting Y_2CCl_2 MXene; (c) the corresponding semiconductor systems; (d) PBE band structure and (e) total density of states for the metallic Y_2CS_2 MXene; and (f) the corresponding metal systems.

As expected, C atoms contribute significantly near the Fermi level, primarily through their p-orbitals. The functionalization elements (chalcogenides and halides) contribute mainly *via* their p-orbitals, while H_2 functionalization contributes through s-orbitals in the same energy region. The electronic properties were calculated using the PBE functional for the metallic systems. In contrast, we employed the HSE06 functional for the semiconductors to obtain more accurate band gap values due to the known underestimation of band gaps by PBE.[41,42] A comparison of the band structures calculated with PBE and HSE06 is shown in Fig. 6.

The fundamental (E_g) and direct (E_g^d) band gaps calculated using HSE06 for the stable semiconductor MXenes are presented in Table 3. Interestingly, none of these monolayers exhibit a direct fundamental band gap. However, in most Y-group monolayers, the difference between E_g and E_g^d is relatively small, typically less than 0.2 eV, except for Y_2CCl_2, where the difference is approximately 0.4 eV. The fundamental band gaps for the Y-group range from 1.24 eV to 1.71 eV, while those for the Sc-group range from 1.65 eV to 1.90 eV. Unlike the Y-group, the Sc-based MXenes exhibit a larger difference between E_g and E_g^d, around 0.4 eV. In both Y and Sc MXenes, we observe that the band gap decreases as the mass of the halide functionalization increases.

3.3 Excitonic and optical properties

Since this study focuses on the excitonic properties of MXenes and their potential for photovoltaic applications, we limit our analysis to the eight stable semiconductor monolayers, as metallic systems cannot be employed as photoabsorbers in solar harvesting devices. Examples of exciton band structures for Y_2CCl_2 and Sc_2CBr_2, along with the quasi-particle effects on the linear optical response *via* the absorption coefficient for all semiconductor MXenes, are shown in Fig. 7 and 8, respectively. The complete dataset for exciton band structures is also provided in the ESI, section S7.†

The exciton band structure helps determine whether the excitonic ground state (Ex_{gs}) is direct or indirect. The excitonic ground state is classified as direct when Ex_{gs} is located at the Γ point, indicating that electron–hole pairs reside at the same *k*-point. An indirect excitonic ground state suggests the possibility of phonon-assisted optical transitions. This may lead to optical excitations lower than the predicted optical band gap, as the latter only accounts for direct transitions. While a thorough investigation of electron–phonon coupling would be necessary for a complete understanding of these cases, such calculations are beyond the scope of this work. Most monolayers display an indirect excitonic ground state, except for Y_2CCl_2, which exhibits a direct excitonic ground state. Ex_{gs} is found between the Γ and M high-symmetry points for the other systems.

The exciton binding energy (Ex_b), defined as the difference between the fundamental band gap (E_g) and the excitonic ground state energy (Ex_{gs}), is presented in Table 3. The binding energies for these systems range from 210 meV to 470 meV in the Y_2CT_2 group and from 270 meV to 400 meV in

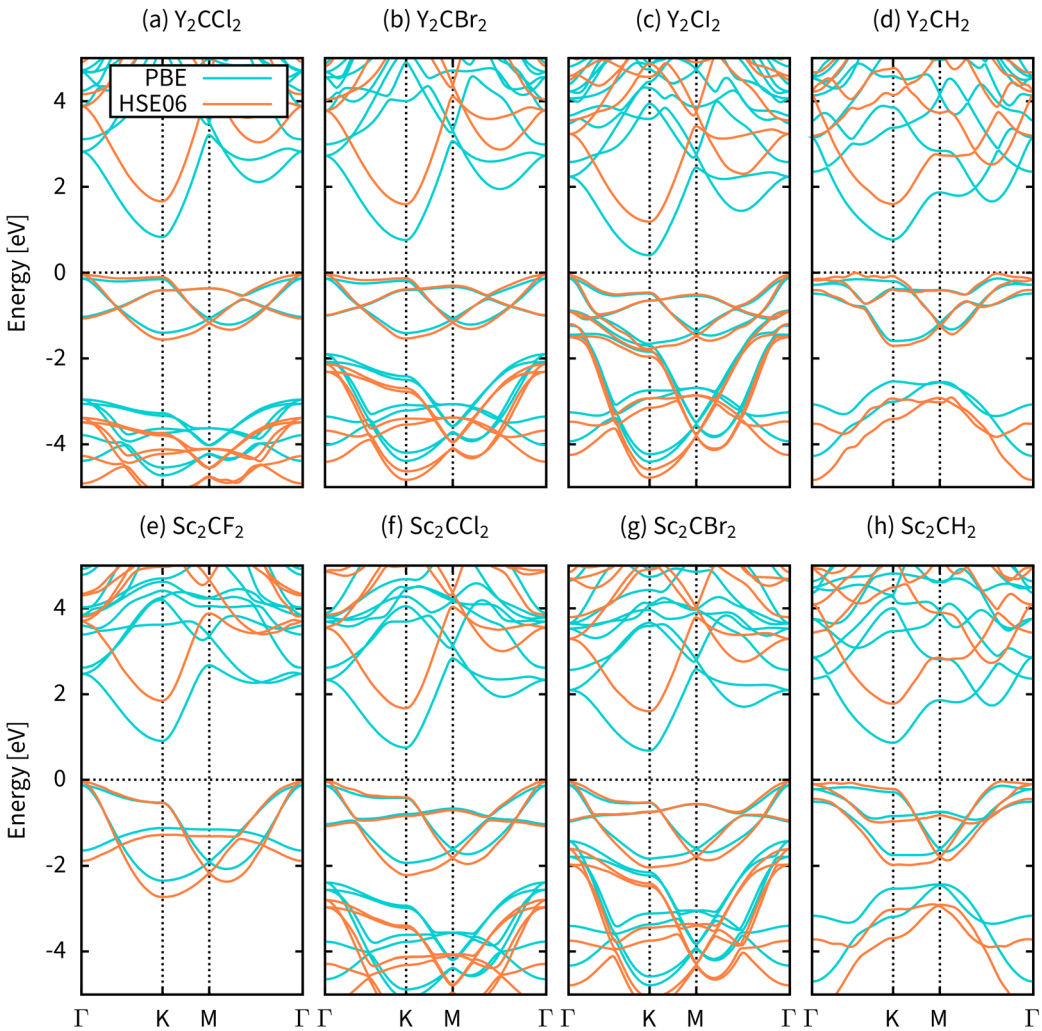

Fig. 6 Electronic band structures of eight monolayers calculated using the PBE (cyan curves) and HSE06 (orange curves) functionals. The panels correspond to: (a) Y_2CCl_2, (b) Y_2CBr_2, (c) Y_2Cl_2, (d) Y_2CH_2, (e) Sc_2CF_2, (f) Sc_2CCl_2, (g) Sc_2CBr_2, and (h) Sc_2CH_2.

Table 3 Excitonic properties obtained using the MLWF-TB + BSE method (HSE06 parametrization): fundamental band gap, E_g (eV); direct band gap, E_g^d (eV); exciton ground state, Ex_{gs} (eV); direct exciton ground state, Ex_{gs}^d (eV); and exciton binding energy, Ex_b (eV), calculated as $E_g - Ex_{gs}$

System	E_g	E_g^d	Ex_{gs}	Ex_{gs}^d	Ex_b
Y_2CCl_2	1.71	1.76	1.34	1.34	0.37
Y_2CBr_2	1.64	1.72	1.29	1.30	0.35
Y_2CI_2	1.24	1.65	1.03	1.24	0.21
Y_2CH_2	1.63	1.69	1.16	1.22	0.47
Sc_2CF_2	1.90	2.39	1.63	2.00	0.27
Sc_2CCl_2	1.71	2.06	1.44	1.68	0.27
Sc_2CBr_2	1.65	2.13	1.41	1.72	0.24
Sc_2CH_2	1.82	1.99	1.42	1.58	0.40

the Sc_2CT_2 group, which is consistent with typical values for 2D monolayers.[58,67] The lowest binding energy is observed for Y_2CI_2, while the highest is found for Y_2CH_2. In the Sc_2CT_2 group, Sc_2CH_2 exhibits the highest binding energy, while the lowest values are observed for Sc_2CF_2 and Sc_2CCl_2. Notably, both groups' largest exciton binding energies are associated with H_2 functionalization, likely due to the passivation of monolayer edges by H atoms, which enhances quantum confinement in the non-periodic direction.

As shown in Fig. 8, the linear optical response of the semiconductor MXene monolayers is calculated at both the BSE (solid curves) and IPA (dashed curves) levels, considering incident linearly polarized light along the $\hat{x}$ (green curves) and $\hat{y}$ directions. As expected, a comparison between the BSE and IPA absorption spectra reveals that excitonic effects induce a significant redshift in the absorption peaks, directly related to the exciton binding energy. Additionally, the spectral shapes differ between BSE and IPA. It is well-known that excitonic effects are sensitive to the proximity of a substrate, which can reduce quasi-particle interactions.[67] In our simulations, the BSE calculations were performed without an external substrate, allowing excitonic effects to manifest fully. In contrast, the IPA model does not account for quasi-particle effects,

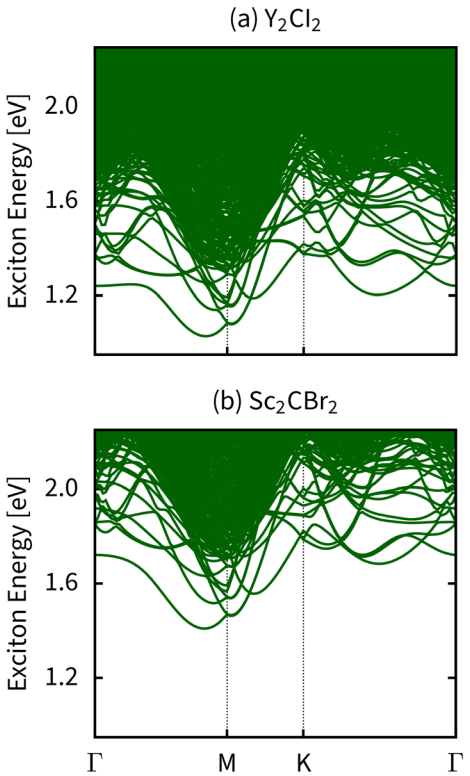

Fig. 7 Exciton band structures along the Γ → M → K → Γ branches for (a) Y_2Cl_2 and (b) Sc_2CBr_2 monolayers.

making the BSE and IPA spectra represent the upper and lower limits of the potential optical response of these materials. The IPA optical band gap matches the direct band gap (E_g^d), while the BSE optical band gap corresponds to the direct excitonic ground state (Ex_{gs}), as shown in Table 3.

The Y_2CT_2 monolayers with T = Cl, Br, I, and H exhibit a primary absorption peak in the infrared (IR) region, along with additional peaks in the visible region, as illustrated in Fig. 8(a)–(d). These monolayers have their optical band gaps in the IR region and demonstrate strong optical responses in the IR, which weaken as the excitation shifts toward the visible and ultraviolet regions. The exception is Y_2CH_2, which shows a strong optical response in the visible region despite its optical band gap being located in the IR. The IPA optical response is nearly isotropic in IR and visible regions, with slight anisotropy appearing in the ultraviolet region. A similar behavior is observed at the BASE level but with weak optical anisotropy in the IR and visible regions. The distinct absorption spectrum of Y_2CH_2 suggests that H functionalization can significantly alter the optical behavior of these MXene monolayers, a trend also seen in the Sc_2CT_2 group.

For the Sc_2CT_2 monolayers (Fig. 8(e)–(h)), the optical band gap redshift occurs from the visible to IR regions as the T functionalization progresses from F to Br. The optical response of Sc_2CCl_2 shows an anisotropic behavior at the BSE level, unlike Sc_2CF_2 and Sc_2CBr_2, which remain isotropic in the IR and visible regions. Despite the higher optical anisotropy in the Sc_2CT_2 group, the overall spectral shape does not differ significantly from that of the Y_2CT_2 group. With H functionalization, optical anisotropy is enhanced in the visible region, where the highest absorption peak is observed. Quasi-particle effects also significantly reduce this compound's optical response in ultraviolet. Although this behavior is present across the Sc_2CT_2 group, the degree of optical anisotropy is lower for other functionalizations.

3.4 Insights into solar harvesting efficiency

PCE is a critical metric in evaluating how effectively a solar cell converts sunlight into electricity. Two main methods for estimating PCE are the Shockley–Queisser (SQ) limit and the spectroscopy-limited maximum efficiency (SLME). The SQ method directly computes PCE (PCE^{SQ}) using the fundamental band gap at the IPA level and the exciton ground state energy at the BSE level. The SLME method (PCE^{SLME}) relies on the total absorption coefficient, which is derived by summing the diagonal components of the dielectric tensor. Additionally, it requires the fundamental and direct band gaps at the IPA level and the exciton ground state and direct exciton ground state energies at the BSE level.

Furthermore, following the approach proposed by Jariwala and co-workers,[68] we calculated the maximum SLME efficiency (PCE_{max}^{SLME}). This metric assumes that all photons with energy equal to or greater than the optical band gap are absorbed, which is theoretically achievable using light-trapping techniques in solar cells.[68] Regardless of the estimation method, it is essential to recognize that these values represent the upper theoretical limit of solar energy conversion efficiency. Achieving these limits experimentally remains challenging, as demonstrated by the progression of perovskite-based cells $MAPbI_3$, where experimental PCE increased from 3.8% to 25.2% over the past decade.[69,70]

Table 4 presents the estimated PCE values for stable semiconductor MXene monolayers, evaluated at different efficiency limits, including the Shockley–Queisser limit (PCE^{SQ}), SLME (PCE^{SLME}), and maximum SLME (PCE_{max}^{SLME}), considering the optical response at both the IPA and BSE levels. For the Y_2CT_2 group, the SQ limit PCE ranges from 19.72% to 28.47% (32.08% to 32.67% at the BSE level), with the discrepancy attributed to the redshift caused by excitonic effects. The exciton ground state energy, around 1.33 eV, is close to the optimal fundamental band gap for maximizing theoretical efficiency in single-junction solar cells.[54] In the Sc_2CT_2 group, PCE^{SQ} varies from 14.48% to 22.63% (22.42% to 30.16% at the BSE level).

The SLME method predicts much lower PCE values, with PCE^{SLME} below 1% for all monolayers, due to the low photon absorbance rates caused by the thin atomic layer thickness of these 2D materials (ranging from 0.78 nm to 1.02 nm). As a result, most incident photons pass through the material without being absorbed. However, when applying the light-trapping scheme proposed by Jariwala *et al.*,[68] which assumes nearly 100% photon absorbance for photons with energy equal to or above the optical band gap, the maximum SLME efficiency (PCE_{max}^{SLME}) for the Y_2CT_2 group ranges from

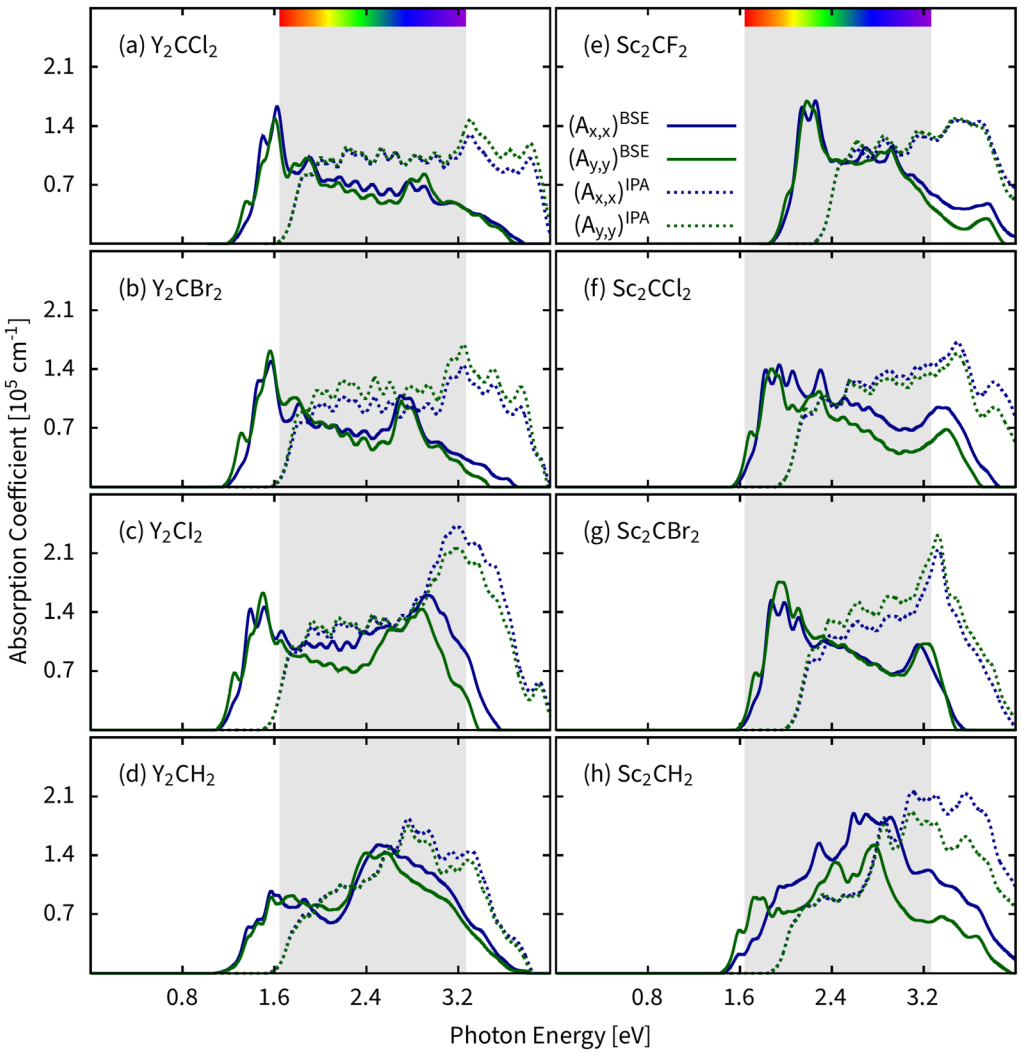

Fig. 8 Optical absorption coefficient spectra of (a) Y_2CCl, (b) Y_2CBr_2, (c) Y_2Cl_2, (d) Y_2CH_2, (e) Sc_2CF_2, (f) Sc_2CCl, (g) Sc_2CBr_2, and (h) Sc_2CH_2 monolayers. Solid lines represent exciton absorption spectra (BSE). In contrast, dashed lines indicate single-particle absorption spectra (IPA), purple curves correspond to the linear optical response for $\hat{x}$ light polarization, and green curves for $\hat{y}$ light polarization.

Table 4 Maximum achieved PCE at the IPA and BSE levels. PCE^{SLME} (%) represents the power conversion efficiency determined by SLME, assuming 100% photon absorbance based on the direct band gap. $PCE_{max}{}^{SLME}$ (%) is the maximum power conversion efficiency obtained under the Shockley–Queisser limit, considering the direct band gap, and PCE^{SQ} (%) , all efficiencies calculated at T = 300 K

	IPA			BSE		
System	PCE^{SLME}	$PCE_{max}{}^{SLME}$	PCE^{SQ}	PCE^{SLME}	$PCE_{max}{}^{SLME}$	PCE^{SQ}
Y_2CCl_2	0.93	26.31	27.32	0.99	32.67	32.67
Y_2CBr_2	0.61	14.10	19.72	1.02	31.73	32.08
Y_2CI_2	0.95	19.62	29.24	1.23	29.85	32.12
Y_2CH_2	0.85	27.14	28.47	0.79	29.85	32.11
Sc_2CF_2	0.37	10.79	14.48	0.57	17.13	22.42
Sc_2CCl_2	0.62	16.59	21.16	0.80	23.25	28.66
Sc_2CBr_2	0.61	14.11	19.72	0.82	21.40	28.05
Sc_2CH_2	0.63	20.16	22.63	0.77	26.06	30.16

14.10% to 27.14% (29.85% to 32.67% at the BSE level). The Sc_2CT_2 group spans from 10.79% to 20.16% (17.13% to 26.06% at the BSE level).

Among the studied systems, the Y_2CT_2 monolayers show greater solar energy than the Sc_2CT_2 systems. Y_2CCl_2 emerges as the most promising photoabsorber, achieving a maximum

SLME efficiency (PCE_{max}^{SLME}) of 32.67% at the BSE level. Conversely, Sc_2CF_2 exhibits the lowest performance, with a PCE_{max}^{SLME} of 17.13%, also at the BSE level.

4 Conclusion

This study employed first principles and semi-empirical methods to investigate the properties of Y- and Sc-based MXene monolayers. Using an automated workflow that integrates five distinct Workflow Active Nodes (WaNos) within the SimStack framework, we found that from the 22 proposed monolayers, 15 were stable or meta-stable from phonon simulations, elastic constants, and AIMD reduced this group to 13 stable monolayers, with eight exhibiting semiconducting behavior. The electronic band gaps of the semiconductors, calculated using HSE06, ranged from 1.24 eV to 1.90 eV, and all displayed indirect band gaps. Our analysis demonstrated that excitonic effects play a pivotal role in determining the optical linear response of these materials. Exciton binding energies, which varied from 210 meV to 470 meV, induced a redshift in the optical band gap, significantly impacting the solar harvesting potential. Some systems achieved solar conversion efficiencies approaching 33% with the inclusion of quasi-particle effects. The Y_2CT_2 and Sc_2CT_2 groups demonstrated solar harvesting efficiencies exceeding 15%, assuming complete absorption of incident light, making them promising candidates for photovoltaic applications. Despite these promising results, challenges remain, particularly in developing viable synthesis methods for these materials and scaling up the production of thin films. Achieving the theoretical upper limits of solar harvesting efficiency will likely require several more years of focused research. Nonetheless, the findings presented here provide valuable insights and a strong foundation for future theoretical and experimental studies on Y- and Sc-based MXene monolayers for solar energy harvesting devices.

Author contributions

B.D.A.H., M.J.P., C.R.C.R., D.G.S.: data curation, software, formal analysis, methodology, funding acquisition, and writing – original draft preparation. M.L.P.J: software, formal analysis, methodology, visualization, funding acquisition, and writing – reviewing. L.A.R.J. and A.C.D.: conceptualization, funding acquisition, and writing – reviewing. All authors reviewed the manuscript.

Data availability

Raw data from our pipeline and additional technical details on using our workflow and the Colab notebook are available in the GitHub repository **https://github.com/KIT-Workflows/MXene-Monolayers**.

The data that support the findings of this study are available from the corresponding author, M.L.P.J., upon reasonable request.

Conflicts of interest

The authors declare that they have no known competing financial interests or personal relationships that could have appeared to influence the work reported in this paper.

Acknowledgements

The authors gratefully acknowledge financial support from the following institutions: the National Council for Scientific and Technological Development (CNPq, grant numbers 307345/2021-1, 408144/2022-0, 305174/2023-1, 350176/2022-1, 444069/2024-0, 444921/2024-9 and 444431/2024-1); the Federal District Research Support Foundation (FAPDF, grant numbers 00193-00001817/2023-43, 00193-00002073/2023-84, 00193-00001807/2023-16, 0193.000942/2015, PDPG-FAPDF-CAPES Centro-Oeste 00193-00000867/2024-94, and PRONEM grant 00193.00001247/2021-20); the Coordination for the Improvement of Higher Education Personnel (CAPES, grant number 88887.005164/2024-00); the Rio Grande do Sul Research Foundation (FAPERGS, grant number 24/2551-0001551-5); and the German Federal Ministry of Education and Research (BMBF) for financial support of the Innovation-Platform MaterialDigital project (**https://www.materialdigital.de**) through funding FKZ number 13XP5094A. The authors also acknowledge computational resources provided by the HoreKa supercomputer, funded by the Ministry of Science, Research, and the Arts Baden-Württemberg and the Federal Ministry of Education and Research; the Santos Dumont supercomputer at the National Laboratory for Scientific Computing; the "Centro Nacional de Processamento de Alto Desempenho em São Paulo" (CENAPAD-SP, UNICAMP/FINEP – MCTI project), supporting projects 570, 634, 897, and 960; Lobo Carneiro HPC (NACAD) at the Federal University of Rio de Janeiro (UFRJ) for project 133; the Ogun Supercomputer at CIMATEC SENAI in Salvador, Bahia; the SDumont supercomputer in the Laboratório Nacional de Computação Científica (LNCC) at Petrópolis-RJ, as part of the ''Sistema Nacional de Processamento de Alto Desempenho" – SINAPAD; and the "Laboratório Central de Processamento de Alto Desempenho" (LCPAD), financed by FINEP through CT-INFRA/UFPR projects.

References

1 K. S. Novoselov, A. K. Geim, S. V. Morozov, D. Jiang, Y. Zhang, S. V. Dubonos, I. V. Grigorieva and A. A. Firsov, *Science*, 2004, **306**, 666–669.

2 V. Shanmugam, R. A. Mensah, K. Babu, S. Gawusu, A. Chanda, Y. Tu, R. E. Neisiany, M. Försth, G. Sas and O. Das, *Part. Part. Syst. Charact.*, 2022, **39**, 2200031.

3 Y. Gogotsi, *MXenes: From Discovery to Applications of Two-Dimensional Metal Carbides and Nitrides*, Jenny Stanford Publishing, 2023.
4 K. Zhang, Y. Feng, F. Wang, Z. Yang and J. Wang, *J. Mater. Chem. C*, 2017, **5**, 11992–12022.
5 X. Ling, H. Wang, S. Huang, F. Xia and M. S. Dresselhaus, *Proc. Natl. Acad. Sci. U. S. A.*, 2015, **112**, 4523–4530.
6 S. Manzeli, D. Ovchinnikov, D. Pasquier, O. V. Yazyev and A. Kis, *Nat. Rev. Mater.*, 2017, **2**, 1–15.
7 M. Naguib, M. Kurtoglu, V. Presser, J. Lu, J. Niu, M. Heon, L. Hultman, Y. Gogotsi and M. W. Barsoum, *Adv. Mater.*, 2011, **23**, 4248–4253.
8 H. Kim and H. N. Alshareef, *ACS Mater. Lett.*, 2019, **2**, 55–70.
9 B. Anasori, Y. Xie, M. Beidaghi, J. Lu, B. C. Hosler, L. Hultman, P. R. C. Kent, Y. Gogotsi and M. W. Barsoum, *ACS Nano*, 2015, **9**, 9507–9516.
10 E. Heidari Semiromi, Z. Khorasani Baghini and A. Mostafaei, *Solid State Commun.*, 2024, **381**, 115451.
11 W. Zeng, X. Ye, Y. Dong, Y. Zhang, C. Sun, T. Zhang, X. Guan and L. Guo, *Coord. Chem. Rev.*, 2024, **508**, 215753.
12 R. B. Rakhi, B. Ahmed, D. Anjum and H. N. Alshareef, *ACS Appl. Mater. Interfaces*, 2016, **8**, 18806–18814.
13 Y. Zhang, N. Zhang and C. Ge, *Materials*, 2018, **11**, 2281.
14 X.-f. Yu, Y.-c. Li, J.-b. Cheng, Z.-b. Liu, Q.-z. Li, W.-z. Li, X. Yang and B. Xiao, *ACS Appl. Mater. Interfaces*, 2015, **7**, 13707–13713.
15 E. Lee, A. VahidMohammadi, Y. S. Yoon, M. Beidaghi and D.-J. Kim, *ACS Sens.*, 2019, **4**, 1603–1611.
16 E. P. Simonenko, N. P. Simonenko, A. S. Mokrushin, T. L. Simonenko, P. Y. Gorobtsov, I. A. Nagornov, G. Korotcenkov, V. V. Sysoev and N. T. Kuznetsov, *Nanomaterials*, 2023, **13**, 850.
17 M. Xin, J. Li, Z. Ma, L. Pan and Y. Shi, *Front. Chem.*, 2020, **8**, 297.
18 L. Verger, V. Natu, M. Carey and M. W. Barsoum, *Trends Chem.*, 2019, **1**, 656–669.
19 K. Li, J. Zhao, A. Zhussupbekova, C. E. Shuck, L. Hughes, Y. Dong, S. Barwich, S. Vaesen, I. V. Shvets, M. Möbius, W. Schmitt, Y. Gogotsi and V. Nicolosi, *Nat. Commun.*, 2022, **13**, 6884.
20 M. K. Aslam, T. S. AlGarni, M. S. Javed, S. S. A. Shah, S. Hussain and M. Xu, *J. Energy Storage*, 2021, **37**, 102478.
21 M. A. Saeed, A. Shahzad, K. Rasool, F. Mateen, J.-M. Oh and J. W. Shim, *Adv. Sci.*, 2022, **9**, 2104743.
22 L. Yin, Y. Li, X. Yao, Y. Wang, L. Jia, Q. Liu, J. Li, Y. Li and D. He, *Nano-Micro Lett.*, 2021, **13**, 1–17.
23 N. Li, J. Peng, W.-J. Ong, T. Ma, Arramel, P. Zhang, J. Jiang, X. Yuan and C. J. Zhang, *Matter*, 2021, **4**, 377–407.
24 N. Talreja, D. Chuahan and M. Ashfaq, *Mater. Adv.*, 2024, **5**, 1454–1461.
25 S. Zhao, W. Kang and J. Xue, *Appl. Phys. Lett.*, 2014, **104**, 133106.
26 A. Mishra, P. Srivastava, A. Carreras, I. Tanaka, H. Mizuseki, K.-R. Lee and A. K. Singh, *J. Phys. Chem. C*, 2017, **121**, 18947–18953.
27 M. Khazaei, M. Arai, T. Sasaki, C. Chung, N. S. Venkataramanan, M. Estili, Y. Sakka and Y. Kawazoe, *Adv. Funct. Mater.*, 2012, **23**, 2185–2192.
28 A. Mishra, S. Satsangi, A. C. Rajan, H. Mizuseki, K.-R. Lee and A. K. Singh, *J. Phys. Chem. Lett.*, 2019, **10**, 780–785.
29 L. Yu and A. Zunger, *Phys. Rev. Lett.*, 2012, **108**, 068701.
30 N. Kumar, M. Kolos, S. Bhattacharya and F. Karlický, *J. Chem. Phys.*, 2024, **160**, 124707.
31 R. Momeni Feili, R. Nejatipour and M. Dadsetani, *Phys. Status Solidi B*, 2022, **260**, 2200469.
32 E. A. Moujaes and A. C. Dias, *J. Phys. Chem. Solids*, 2023, **182**, 111573.
33 D. Guedes-Sobrinho, C. R. Caldeira Rêgo, G. R. Da Silva, H. R. Da Silva, W. Wenzel, M. J. Piotrowski and A. Cavalheiro Dias, *J. Phys. Chem. C*, 2024, **128**, 7242–7251.
34 C. R. C. Rêgo, J. Schaarschmidt, T. Schlöder, M. Penaloza-Amion, S. Bag, T. Neumann, T. Strunk and W. Wenzel, *Front. Mater.*, 2022, **9**, 877597.
35 J. Schaarschmidt, J. Yuan, T. Strunk, I. Kondov, S. P. Huber, G. Pizzi, L. Kahle, F. T. Bölle, I. E. Castelli, T. Vegge, *et al.*, *Adv. Energy Mater.*, 2022, **12**, 2102638.
36 P. Hohenberg and W. Kohn, *Phys. Rev.*, 1964, **136**, B864–B871.
37 W. Kohn and L. J. Sham, *Phys. Rev.*, 1965, **140**, A1133–A1138.
38 G. Kresse and J. Furthmüller, *Phys. Rev. B:Condens. Matter Mater. Phys.*, 1996, **54**, 11169–11186.
39 P. E. Blöchl, *Phys. Rev. B:Condens. Matter Mater. Phys.*, 1994, **50**, 17953–17979.
40 J. P. Perdew, K. Burke and M. Ernzerhof, *Phys. Rev. Lett.*, 1996, **77**, 3865–3868.
41 A. J. Cohen, P. Mori-Sánchez and W. Yang, *Phys. Rev. B: Condens. Matter Mater. Phys.*, 2008, **77**, 115123.
42 J. M. Crowley, J. Tahir-Kheli and W. A. Goddard, *J. Phys. Chem. Lett.*, 2016, **7**, 1198–1203.
43 C. R. C. Rêgo, P. Tereshchuk, L. N. Oliveira and J. L. F. Da Silva, *Phys. Rev. B*, 2017, **95**, 235422.
44 J. Heyd and G. E. Scuseria, *J. Chem. Phys.*, 2004, **121**, 1187–1192.
45 M. Gajdoš, K. Hummer, G. Kresse, J. Furthmüller and F. Bechstedt, *Phys. Rev. B:Condens. Matter Mater. Phys.*, 2006, **73**, 045112.
46 A. Togo and I. Tanaka, *Scr. Mater.*, 2015, **108**, 1–5.
47 K. Momma and F. Izumi, *J. Appl. Crystallogr.*, 2008, **41**, 653–658.
48 V. Blum, R. Gehrke, F. Hanke, P. Havu, V. Havu, X. Ren, K. Reuter and M. Scheffler, *Comput. Phys. Commun.*, 2009, **180**, 2175–2196.
49 V. Havu, V. Blum, P. Havu and M. Scheffler, *J. Comput. Phys.*, 2009, **228**, 8367–8379.
50 A. C. Dias, J. F. Silveira and F. Qu, *Comput. Phys. Commun.*, 2023, **285**, 108636.
51 E. E. Salpeter and H. A. Bethe, *Phys. Rev.*, 1951, **84**, 1232–1242.
52 A. A. Mostofi, J. R. Yates, Y.-S. Lee, I. Souza, D. Vanderbilt and N. Marzari, *Comput. Phys. Commun.*, 2008, **178**, 685–699.

53 C. A. Rozzi, D. Varsano, A. Marini, E. K. U. Gross and A. Rubio, *Phys. Rev. B:Condens. Matter Mater. Phys.*, 2006, **73**, 205119.
54 W. Shockley and H. J. Queisser, *J. Appl. Phys.*, 1961, **32**, 510–519.
55 ASTM-G173–03, *Standard Tables for Reference Solar Spectral Irradiances: Direct Normal and Hemispherical on 37° Tilted Surface*, ASTM International, West Conshohocken, PA, 2012, DOI: **10.1520/g0173-03r20**.
56 J. F. R. V. Silveira, R. Besse, A. C. Dias, N. A. M. S. Caturello and J. L. F. D. Silva, *J. Phys. Chem. C*, 2022, **126**, 9173–9184.
57 A. C. Dias, H. Bragança, M. P. Lima and J. L. F. Da Silva, *Phys. Rev. Mater.*, 2022, **6**, 054001.
58 A. Cavalheiro Dias, C. D. Almeida Cornélio, M. J. Piotrowski, L. A. Ribeiro Júnior, C. M. de Oliveira Bastos, C. R. Caldeira Rêgo and D. Guedes-Sobrinho, *ACS Appl. Energy Mater.*, 2024, **7**, 8572–8582.
59 M. Bernardi, M. Palummo and J. C. Grossman, *Nano Lett.*, 2013, **13**, 3664.
60 R. Gaudoin, W. M. C. Foulkes and G. Rajagopal, *J. Phys.: Condens. Matter*, 2002, **14**, 8787–8793.
61 N. Modi, Y. Naik, P. Parmar, P. Jariwala, D. Shah and P. Thakor, *Mater. Today: Proc.*, 2023, DOI: **10.1016/j.matpr.2023.01.344**.
62 Y. Jiang, Y. Zhang, Q. Huang, L. Hao and S. Du, *J. Mater. Res. Technol.*, 2020, **9**, 14979–14989.
63 G. K. Inui, J. F. R. V. Silveira, A. C. Dias, R. Besse and J. L. F. Da Silva, *J. Phys.: Condens. Matter*, 2022, **34**, 305703.
64 T. Hu, F. Jia, G. Zhao, J. Wu, A. Stroppa and W. Ren, *Phys. Rev. B*, 2018, **97**, 235404.
65 X. Zhang, X.-F. Qiao, W. Shi, J.-B. Wu, D.-S. Jiang and P.-H. Tan, *Chem. Soc. Rev.*, 2015, **44**, 2757–2785.
66 Y. He, *J. Alloys Compd.*, 2016, **654**, 180–184.
67 A. C. Dias, H. Bragança, J. P. A. de Mendonça and J. L. F. Da Silva, *ACS Appl. Energy Mater.*, 2021, **4**, 3265–3278.
68 D. Jariwala, A. R. Davoyan, J. Wong and H. A. Atwater, *ACS Photonics*, 2017, **4**, 2962–2970.
69 A. Kojima, K. Teshima, Y. Shirai and T. Miyasaka, *J. Am. Chem. Soc.*, 2009, **131**, 6050–6051.
70 L. A. Frolova, A. I. Davlethanov, N. N. Dremova, I. Zhidkov, A. F. Akbulatov, E. Z. Kurmaev, S. M. Aldoshin, K. J. Stevenson and P. A. Troshin, *J. Phys. Chem. Lett.*, 2020, **11**, 6772–6778.